

FEATURE ARTICLE

Structure Analysis of Nanowires and Nanobelts by Transmission Electron Microscopy

Yong Ding and Zhong Lin Wang*

*School of Materials Science and Engineering, Georgia Institute of Technology, Atlanta, Georgia 30332-0245**Received: April 27, 2004; In Final Form: June 13, 2004*

One-dimensional (1D) nanostructures, such as nanowires, nanobelts, and nanorods, are attracting a great deal of research interest due to their unique properties and novel applications. Structure analysis of 1D nanostructures is an essential part of research because achieving structural control is the key step in controlling properties and device performances. Using ZnO, CdSe, and ZnS as examples, this work addresses the technical details of how to use transmission electron microscopy to correctly analyze the structure of nanowires and nanobelts, including growth direction, side/top surfaces, surface polar direction, surface reconstruction, point defects, dislocations, planar defects, and twin/bicrystal structures. The methodologies introduced can be applied to a wide range of 1D nanostructures.

1. Introduction

One-dimensional (1D) and quasi-one-dimensional nanostructures are attracting a great deal of attention due to their unique properties and novel applications.^{1,2} Besides carbon tubular structures, a variety of nanostructures have been synthesized, including cages,^{3–5} cylindrical wires,^{6–10} rods,^{11–14} nails,¹⁵ coaxial¹⁶ and bi-axial cables,¹⁷ ribbons or belts,^{18,19} sheets,²⁰ diskettes,²¹ springs,²² rings,²³ propellers,²⁴ and more. These novel structures have semiconductive, ferroelectric, magnetic, and/or piezoelectric properties and are of great importance to nanotechnology. It is well-known that a single-walled carbon nanotube can be metallic or semiconductive, depending on the helical angle at which the graphitic sheet is rolled up. It is unfortunate that synthesis of nanotubes with controlled helical angles is not feasible. For 1D nanostructures, especially when their diameter reaches a few nanometers, it is expected that the properties could be strongly affected by the structure of the side surfaces. For applications, it is important to determine the surface structure of 1D nanostructures.

Transmission electron microscopy (TEM), as one of the most powerful tools in nanotechnology, has played an important role in characterizing 1D nanostructures, not only in determining crystal and surface structure, but also chemical structure. The objective of this feature article is to address the issues related to structure analysis of 1D nanostructures by TEM, including growth direction, side surfaces, polar-direction, surface reconstruction, defect structures, and twin/bicrystal structures. The goal is to illustrate the principles and technical details of applying TEM to correctly characterize the 1D nanostructures. This paper is exclusively about nanowires and nanobelts. Structure analysis of nanotubes has been described systematically elsewhere.²⁵

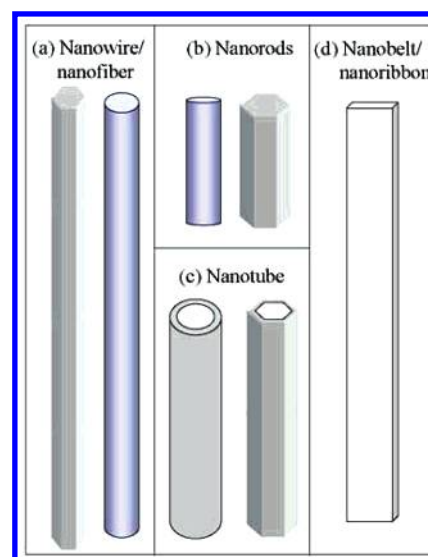


Figure 1. Typical morphologies of one-dimensional nanostructures: nanowires, nanorods, nanotubes, and nanobelts.

2. General Morphology of 1D Nanostructures

In the literature, there are a few names being used for describing 1D nanostructures, such as nanorod, nanowire, nanofiber, nanobelts, and nanoribbon etc. Nanowires usually means a linear structure that has specific growth direction, but its side surfaces and shape of cross-section may not be well defined or uniform (Figure 1a). less restriction about the shape of the cross-section and uniformity broadens the family of nanowires to include more nanostructures. But for achieving property control, it is important to clearly define the side surfaces of a nanowire. A nanorod is a nanowire with a shorter length (Figure 1b). A nanotube is a 1D nanostructure with a hollow interior channel (Figure 1c). Nanobelts/nanoribbons are 1D nanostructures with well-defined side facets (Figure 1d), and they have more restrictive shape and uniformity than the nanowires.

* To whom correspondence should be addressed. E-mail: zhong.wang@mse.gatech.edu.

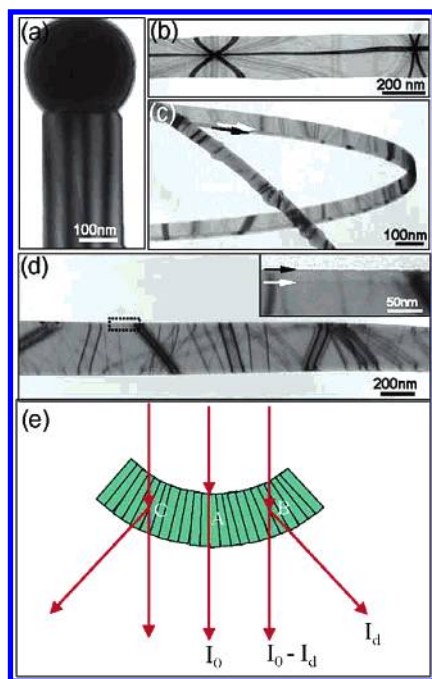


Figure 2. (a) TEM image of Sn catalyzed ZnO nanowire, showing diffraction effect produced thickness fringes across the width of the nanowire. (b,c) TEM images of ZnO nanobelts, showing the bending contours. After tilting the specimen, the up surface of the belt can be seen in (d). (e) Schematic model about the formation of bending contour.

3. Thickness Fringes and Bending Contours in Imaging Nanowires and Nanobelts

For single crystal 1D nanostructures, electron diffraction by the crystal lattice produces various contrasts. Thickness fringes are created by a change in the projected thickness of the nanowire across its diameter (Figure 2a). To understand the thickness fringes, the two-beam diffracting condition is used, simplifying this discussion, one is the transmitted electron beam, and the other is the diffracted beam. An increase in crystal thickness results in an oscillation of the diffracted beam due to the multiple-scattering effect, producing the thickness fringes. The corresponding change in crystal thickness for the two adjacent thickness fringes is a few tens of nanometers. Using thickness fringes, one may identify the symmetry of the nanowire. For a straight and uniform nanowire, the projected thickness along each fringe is constant. But for nanowires with thicknesses smaller than a few tens of nanometers, no thickness fringes would be observed.

Bending contour is another typical contrast, which is most frequently observed in bright-field TEM imaging of nanobelts, as shown in Figure 2b–d. The physics of bending contour is due to a variation of atomic plane in respect to the direction of the incident electron beam (Figure 2e). Due to the crystal bending, the same family of atomic planes of the specimen may have different orientations, thus the angle between the incident electron beam and the local atomic plane changes across the specimen. If the beam is parallel to the atomic plane at point A in Figure 2e, for example, then there is little diffraction effect, and the TEM image shows bright contrast. At point B, the incident beam may strike the atomic plane at the Bragg angle, strong diffraction is created, and thus, the TEM image of the local area would show darker contrast. The contrast is closely associated with the local symmetry, and in some cases, three-dimensional (3D) bending can show “s” shape of contrast, as presented in Figure 2b, the center of which corresponds to the

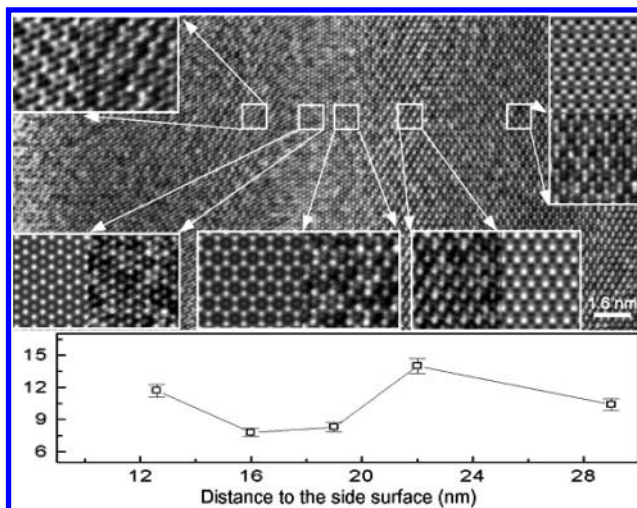


Figure 3. Determination of local thickness by high-resolution TEM. HRTEM image of a ZnO nanobelt shows the dependence of image contrast on local sample thickness. The insets are the grouped experimental image together with the corresponding simulated image. A plot of the local thickness (nm) determined by the technique from several spots away from the edge of the nanobelt.

zone axis of the crystal. Bending contour is especially pronounced in oxide nanostructures.

4. Thickness of Nanobelts

Determination of crystal thickness by TEM is challenging, especially when the sample thickness is a few nanometers. By depositing a nanostructure onto a flat solid substrate, atomic force microscopy can be applied to measure the thickness. For nanobelts thicker than 50 nm, convergent beam electron diffraction (CBED) may be applied to measure its thickness.²⁶ In some cases, tilting a nanobelt may derive its thickness. The inset in Figure 2d is a ZnO nanobelt after being tilted for $\sim 20^\circ$, showing the projected thickness side at the edge. The nanobelt thickness can be calculated based on the projection TEM image and the sample-tilting angle. For nanobelts or nanowires thinner than 20 nm, quantitative comparison of the experimental high-resolution TEM image with the simulated image can give the crystal thickness.

Figure 3 is a quantitative comparison of high-resolution TEM (HRTEM) image recorded from a ZnO nanobelt with the theoretically simulated images. The HRTEM image was recorded at 400 kV from a *c*-plane dominated [01 $\bar{1}$ 0] growth ZnO nanobelt. Besides a small distortion in the orientation of the nanobelt across its width, quantitative comparison between the observed image in the local region can be compared with the simulated image by changing crystal thickness, as grouped in Figure 3. The detailed contrast along the atomic columns in the HRTEM image in local areas changes with the variation of the local thickness, which provides an effective technique for determining nanobelt thickness less than 20 nm. The HRTEM images from the five rectangles enclosed areas are enlarged in the insets of Figure 3, and the best matched images from simulation are displayed side-to-side. The simulation was for spherical aberration $C_s = 0.5$ mm and under Scherzer defocus condition. The determined thickness is potted at the lower part of Figure 3 as a function of the distance from the edge of the nanobelt. An error of less than 1 nm has been achieved.

5. Growth Direction of Nanowires and Nanobelts

Combining TEM images with corresponding electron diffraction patterns is a key in structure analysis. When determining

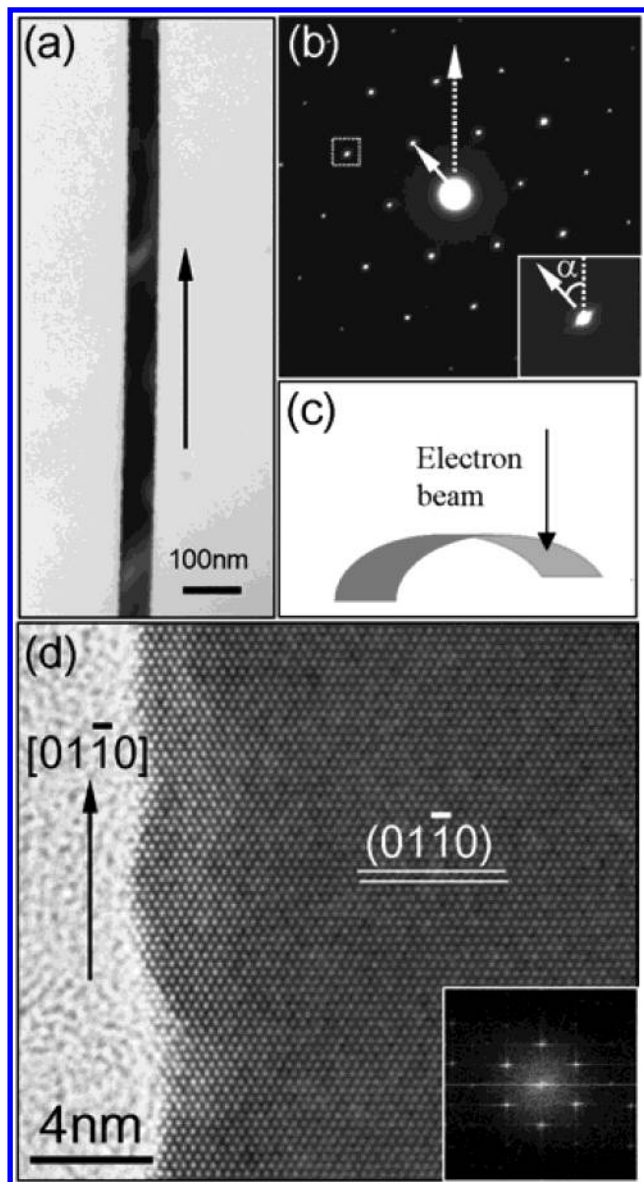


Figure 4. Magnetic rotation angle and determination of the growth direction of a nanowire/nanobelt. (a) TEM image of a ZnO nanobelt and (b) its corresponding selected area electron diffraction (SAED) pattern. The streaking of the spot in the inset of (b) is due to the sharp edge of the nanowire, which can be used to correct the magnetic rotation angle between the image and the diffraction pattern. (c) Schematic diagram showing the folded shape of a nanobelt and the incident electron beam, showing the possibility of incorrect determination of growth direction. (d) HRTEM image from the nanobelt shown in (a), and its Fourier transform.

the growth direction of a 1D nanostructure, it is important to ensure that the incident electron beam is perpendicular to the growth direction. By depositing 1D nanostructures on a TEM grid, there is no guarantee that the nanowire will be flat on the substrate. A reliable way is to measure at least dozens of nanobelts to see if the determined growth directions are unique and self-consistent. If not, then one must carefully check the data to judge if there is more than one growth direction.

The operation of TEM relies on magnetic lenses, and Lorentz force results in an instrument determined rotation between the recorded diffraction pattern and the image due to a change in optical mode. For newly built equipment, manufactured at least in the last 10 years, this rotation effect has been automatically corrected by compensating optics, but for older instruments, this rotation does exist. Figure 4(a) is a bright-field TEM image of

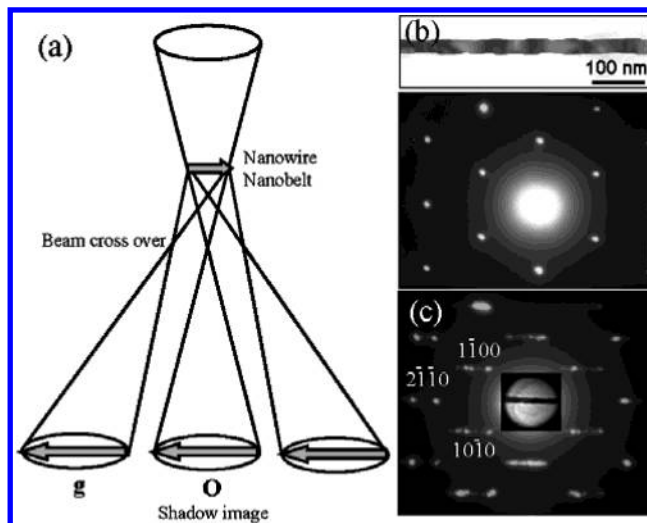


Figure 5. Shadow image technique for determining the growth direction of a nanowire/nanobelt. (a) Optical diagram for shadow imaging. (b) TEM image and the SAED pattern from a nanobelt. (c) The corresponding shadow image recorded in diffraction mode.

a ZnO nanowire recorded at 400 kV using a JEOL 4000EX, which has the rotation effect. After tilting the specimen perpendicular to the electron beam, the selected-area diffraction (SAED) pattern from the nanowire is recorded and is shown in Figure 4b without any correction in rotation angle. The diffraction pattern is $[0001]$, but the nanowire direction is not pointing to any low index diffraction spot in the pattern. This is caused by the magnetic rotation between the image and the diffraction pattern.

If the magnetic rotation angle between the image and the SAED pattern is known, then the growth direction can be easily determined from the SAED pattern. If the rotation angle is unknown, then a simple technique can be applied to determine its value. The principle relies on the shape factor introduced by the sharp edge of the 1D nanostructure in the electron diffraction pattern. Considering the shape effect of the nanowire, a streaking would be produced in the diffraction pattern along a direction perpendicular to the nanobelt direction, as shown by the enlarged diffraction spot inserted in Figure 4b. The rotation angle α determined is applied to define the growth direction of the nanowire, which is concluded to be $[01\bar{1}0]$.

The most direct method is using HRTEM image of the nanobelt and its Fourier transform for determining the nanowire growth direction. Figure 4d is a HRTEM image of the nanobelt shown in Figure 4a. The Fourier transform of the image directly gives the growth direction of the nanobelt being $[01\bar{1}0]$.

Shadow imaging is another technique for determining the nanowire growth direction. Using a field emission TEM and converging the electron beam onto the nanobelt, the image and the converged beam diffraction pattern can be captured simultaneously in the diffraction mode (Figure 5a), simply by changing the beam convergence and using the brightness control knob so that the beam cross over is under/over the object. In this case, the index of the diffraction spot g that is parallel to the nanobelt is the growth direction, provided the incident beam is perpendicular to the nanowire. Figure 5b is an TEM image and the corresponding SAED pattern from a ZnO nanobelt. By increasing the beam convergence, the shadow image of the nanobelt is shown in the diffraction pattern (Figure 5c), which is pointing to the $[2\bar{1}10]$ direction, the nanobelt growth direction.

Another technique for directly determining the nanobelt growth direction is presented in Figure 6. The first step is to

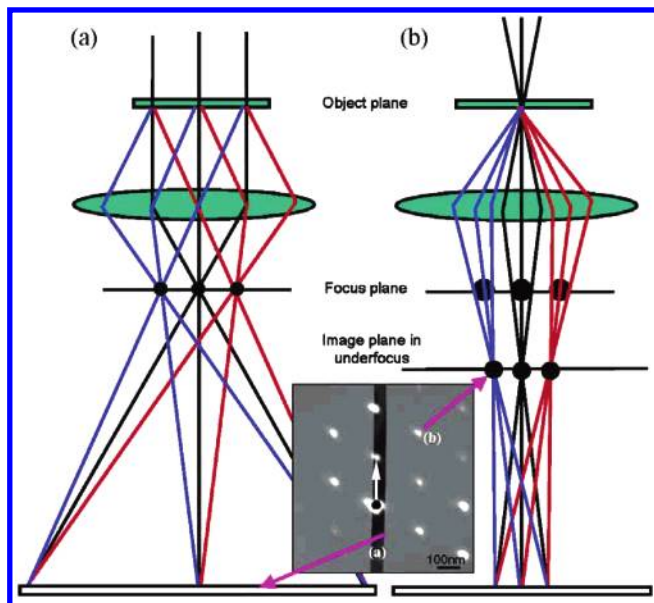


Figure 6. Determination of nanowire/nanobelt growth direction. (a) Optical diagram for receiving the imaging of a nanowire under parallel beam illumination. (b) Optical diagram for recording the diffraction information from the nanowire in the *imaging mode* by converging the electron beam and under-focusing the objective lens, so that the diffraction pattern appears in the image mode. The image shown is a double-exposed image and “diffraction pattern” recorded at the optical configurations of (a) and (b).

form a bright field TEM image using a parallel illumination beam and record the image at in-focus condition (Figure 6a). The second step is to converge the beam onto the specimen, then to underfocus the objective lens so much that the diffraction spots appear in the image mode (Figure 6b). The next step is to record the image onto the same film. The index of the diffraction spot parallel to the nanobelt is the growth direction.

6. Indexing Growth Direction and Growth Front Plane

After correctly determining the nanowire growth direction, it is necessary to align the image with the diffraction pattern so that the information in real space is consistent to that provided by reciprocal space. For example, if the ZnO nanowire growth is along $[0001]$, it is necessary to point the (0001) diffraction spot parallel to the nanowire growth direction when composing figures. Misaligned images and diffraction patterns are poor representation but, unfortunately, are frequently found in the literature!

For cubic structures, the Miller index for a crystal plane is the same as that for its normal direction. It must be pointed out that, for noncubic structure systems, the Miller index for nanowire growth direction may not be the same as the Miller index for the corresponding atomic plane perpendicular to the nanowire. Taking the rutile structured SnO_2 nanobelt as an example, the normal direction of the wide surface of the ribbon is $[102]$, but the surface plane is close to $(10\bar{1})$ crystallographic plane (note: SnO_2 has a tetragonal lattice structure). The axial growth plane is (201) , but the growth direction is close to $[101]$.²⁷ One must carefully examine the crystal structure case by case.

7. Side Surfaces of Nanowires and Nanobelts

Determination of the side surfaces of a nanowire is not trivial. For a general case, the side surfaces of the as-grown nanowires that were imaged depend on the direction of the incident electron

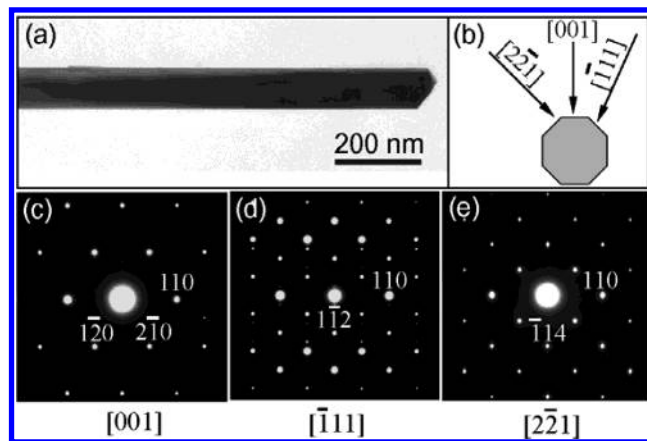


Figure 7. Determination of the side surfaces of a nanowire. (a) Low magnification TEM image of a $\alpha\text{-Fe}_2\text{O}_3$ nanowire. (b) Three possible incident electron beam directions for imaging the nanowire, and (c–e) are the corresponding diffraction pattern along the three zone axes.

beam. Figure 7a is a TEM image of a $\alpha\text{-Fe}_2\text{O}_3$ nanowire growing along $[110]$. Three different patterns were received for each direction of the incident electron beam; is $[001]$, $[\bar{1}11]$ or $[2\bar{2}1]$ (Figure 7b–e). A common characteristic of the three patterns was that the (110) spot appears in all of them, because the incident beam was perpendicular to the nanowire. A reliable approach is to examine many nanowires and get a statistical distribution about the observed facets.

The most direct way for determining the side surfaces is to prepare cross-section samples of nanowires and image them directly along the nanowire direction.²⁸ The sample can be prepared by embedding nanowires in a conductive epoxy, and cross-section sample can be made by slicing thin sections using an ultramicrotome. Some of the nanowires with growth directions closely parallel to the incident electron beam can be found in TEM, thus the side surfaces can be determined by either electron diffraction or HRTEM.

In some cases, determination of side surfaces needs a conjunction use of several techniques. Gold nanorods, for example, can have $\{110\}$ type side surfaces, which are unusual for face-centered cubic metals.²⁹ HRTEM, electron diffraction and dark-field TEM images with thickness fringes have been co-applied to determine the surfaces.

8. Polar-Direction of Nanobelts

Some crystal surfaces have polarity that is produced by the atomic termination on the surface. Take the wurtzite structured ZnO as an example, it can be viewed as a number of alternating planes composed of tetrahedrally coordinated O^{2-} and Zn^{2+} ions, stacked alternatively along the c -axis. The oppositely charged ions produce positively charged $(0001)\text{-Zn}$ and negatively charged $(000\bar{1})\text{-O}$ polar surfaces, resulting in a normal dipole moment and spontaneous polarization along the c -axis. Experimentally determining if the surface terminates with Zn or oxygen is important for understanding the polar surface dominated growth phenomena. From kinematic scattering theory, such as for X-rays, the polar surfaces cannot be determined because the diffraction intensities for the $+\mathbf{g}$ and $-\mathbf{g}$ diffraction spots are identical. In this case, the convergent beam electron diffraction (CBED) with strong dynamic diffraction effect is a unique tool used to answer this question.

CBED patterns are formed with a converged electron probe illuminating the sample area, which can be as small as a few nanometers. The convergence angle is equivalent to imaging the crystal through a range of directions, so it is sensitive to

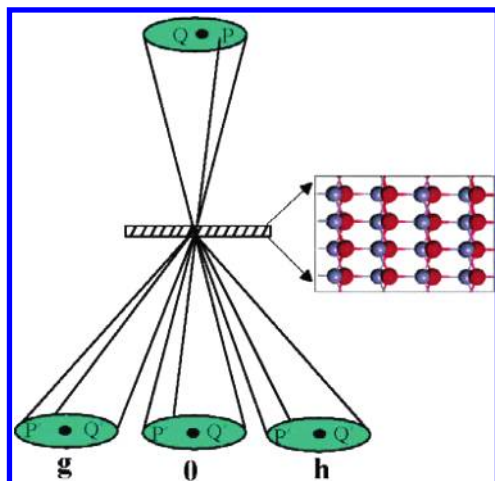


Figure 8. Ray diagram of convergent beam electron diffraction for determining the polarization of ZnO.

the 3D crystal structure of the sample. The beam convergence determines the size of the diffraction disks. The cross point of the converged beam can be at or below the specimen, depending on the quality of the specimen and the required convergence angle. The incident probe consists of many plane-wave components propagating along different directions, thus forming a converged conical electron probe (Figure 8). For an incident beam P, diffraction results in a complete point diffraction pattern consisting of P's as ruled by the Bragg reflection law. A similar set of point diffraction pattern is formed for another plane-wave component Q. Therefore, for cases where there are no disk overlaps, a perfect registration is retained between each incident beam direction and the diffracted beams. The intensity distribution in the disks in the CBED pattern contains the local symmetry and point group information of the electron beam illustrated area.³⁰ More details and procedures have been given by Spence and Zuo,³¹ Buxton et al.,³² and Tanaka et al.³³

A key requirement for forming high quality CBED pattern is the sample thickness, which has to be sufficiently large to give strong dynamic effect. Figure 9(a) shows a ZnO comb nanostructure. The SAED pattern in Figure 9b indicates the teeth of the comb grow asymmetrically along positive and negative c directions, But which direction is the positive direction remains to be determined. The CBED pattern recorded from the comb in Figure 9c shows asymmetry intensity distribution in the disks along the $\pm c$ directions. The CBED pattern can be quantitatively simulated based on the well-established dynamic electron diffraction theories.³¹ Using the crystal structure of ZnO, by defining the incident beam geometry, and adjusting the crystal thickness to match the experimental pattern, a theoretically calculated pattern is given in Figure 9d. Comparing the simulated with the experimental patterns, the polar surfaces are uniquely determined. The results indicate that the teeth grow along $[0001]$ on the Zn-terminated (0001) surface.^{34,35} The oxygen-terminated $(000\bar{1})$ surface is chemically inert. The asymmetric catalytic behavior of the two oppositely charged surfaces results in the formation of comb structure.

9. Helical and Zigzag Structures

It is known that TEM images provide two-dimensional (2D), thickness projected structure information of an object. Careful examination of the TEM images could still reveal a bit of 3D structure. We use the helical and zigzag structures as examples. Figure 10a–c shows three TEM images recorded from three different types of structures of ZnO: in-plane zigzag structure

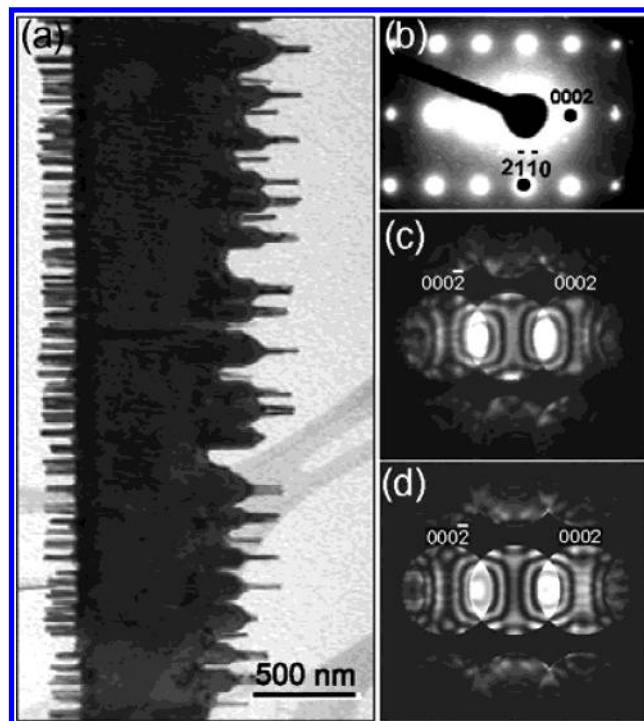


Figure 9. Polar surface induced anisotropic growth. (a) TEM image of a ZnO comb structure and (b) the corresponding SAED pattern. (c) and (d) are experimental and simulated CBED pattern of the ZnO comb.

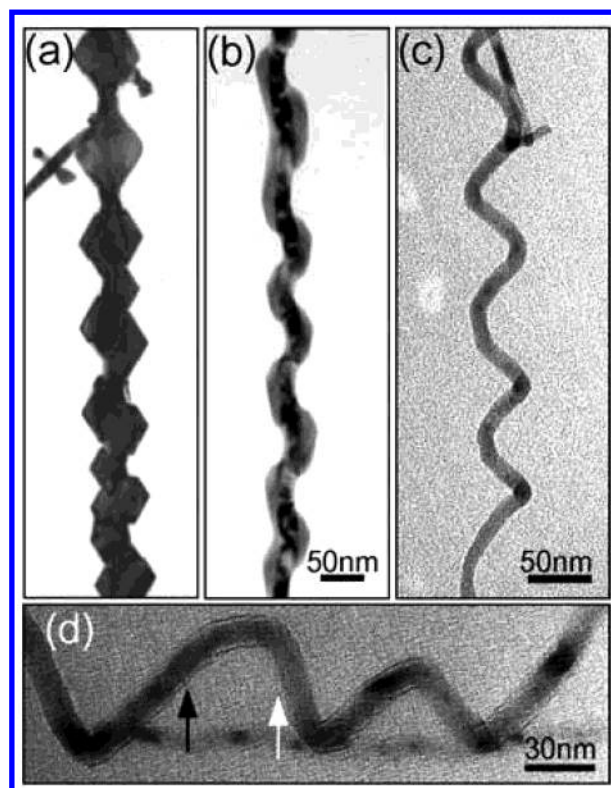


Figure 10. Identification of 3D helical structures. TEM images of (a) a zigzag ZnO structure produced by swing of growth direction between $[1010]$ and $[01\bar{1}0]$, (b) a false spring structure and (c) ZnO helix. (d) An enlargement of a segment of the structure shown in (c).

induced by a periodic change in growth directions; a helical structure of a nearly straight ZnO nanowire surrounded by an amorphous layer with a periodically "etched" helical concave during growth; and a spring structure. Among the three images, only the nanospring in Figure 10c is a 3D coiling of a thin nanowire.³⁶ This is identified through the image contrast at the

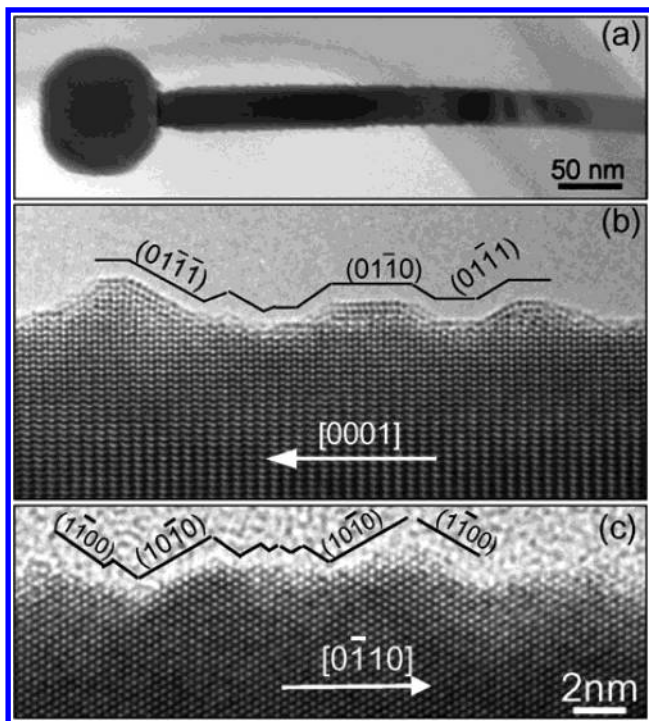


Figure 11. Profile TEM imaging of reconstructed surfaces. (a) Low magnification and (b) high-resolution TEM images of a ZnO nanowire growing along $[0001]$, and (c) HRTEM image of a nanobelt growing along $[0110]$, showing surface reconstruction and tiny facets.

edge of the nanowire. Changing in contrast is possible by changing the focus of the objective lens. The segment of the nanowire lying on the focal plane shows minimum contrast (see the region indicated by a white arrowhead in Figure 10d), while that away from focus shows dark-white fringes at the edge of the nanowire (see the region indicated by a black arrowhead in Figure 10d), reflecting the 3D shape of the coiling structure.

10. Surface Reconstruction

Large surface-to-volume ratio is the most typical characteristic of all of the nanomaterials. A larger percentage of dangling bonds on surfaces produce new surface structures, which are called reconstruction. For a crystalline material, the surfaces are usually dominated by some low index facets, such as $\{111\}$ and $\{100\}$ for gold.³⁷ Although scanning tunneling microscopy is a powerful method for studying surface reconstruction of large surfaces,³⁸ direct imaging of surfaces of nanostructures at atomic resolution still requires HRTEM. By imaging a nanostructure in profile, the reconstruction of the surfaces parallel to the incident electron beam can be revealed.

Figure 11(a) is a low magnification TEM image of a ZnO nanowire that grows along $[0001]$ with an Sn particle at its tip.³⁹ The reconstruction of the $(01\bar{1}0)$ side surfaces is presented in Figure 11b. Besides the $(01\bar{1}0)$ planes, $(01\bar{1}1)$ and $(01\bar{1}\bar{1})$ facets are observed. The nanobelt shown in Figure 11c grows along $[0110]$ direction, the top/bottom and side surfaces are $\pm(0001)$ and $\pm(2\bar{1}\bar{1}0)$ planes, respectively. While zooming in the upside surface, it can be found that the $(2\bar{1}\bar{1}0)$ plane are not smooth and reconstructed into a series of (1100) and (1010) facets.

11. Structures of Catalyst Particles in Vapor–Liquid–Solid (VLS) Growth

The vapor–liquid–solid (VLS) process has been an important approach in growth of quasi-one-dimensional nanowires/nanotubes.⁴⁰ In the VLS process, a metal catalyst is rationally chosen

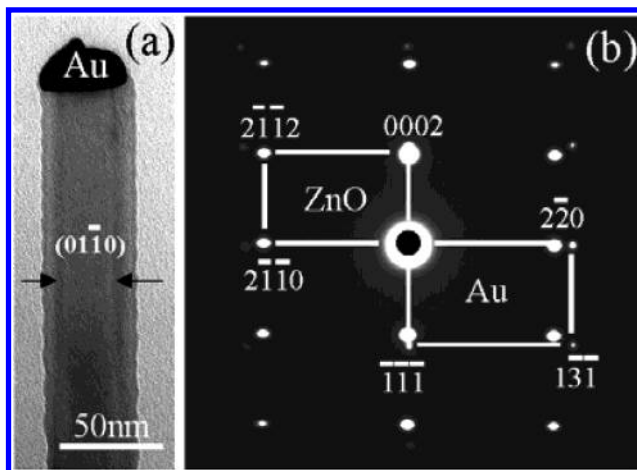


Figure 12. Orientation relationship between catalyst particle and the grown nanowire. (a) TEM image of Au catalyzed ZnO nanowire, (b) the SAED pattern including both Au catalyst and ZnO nanowire.

from the phase diagram by identifying a metal that is in liquid at the growth temperature and serves as the site for adsorbing the incoming molecules, but the metal does not form a solid solution with the nanowire, thus it is phase separated at the growth front and leads the growth. The metal liquid droplet serves as a preferential site for absorption of gas-phase reactant. Nanowire growth begins after the liquid becomes supersaturated in reactant materials and continues as long as the catalyst alloy remains in a liquid state and the reactant is available.⁴¹ During the growth, the catalyst droplet directs the nanowire's growth direction and defines the diameter of the nanowire. As a result, the nanowires obtained from the VLS process typically have a solid catalyst nanoparticle at the ends with sizes comparable to diameters of the connected nanowires. Metal particles such as Au and Fe are effective for growing nanowires of Si,⁴² III–V compound, II–VI compound, and oxide: such as Au/ZnO,⁴³ Fe/SiO₂,⁴⁴ Co/SiO₂,⁴⁵ Ni/Ga₂O₃,⁴⁶ Ga/SiO₂.⁴⁷

It has been found that sometimes the catalyst particles have a fixed orientation relationship with their guided nanowires or nanobelts. The ZnO nanowire in Figure 12(a) is guided by an Au catalyst particle. The incident electron beam was $[01\bar{1}0]$ of ZnO. The thickness contrast indicates the surfaces of the nanowire are composed by six $\{01\bar{1}0\}$ facets. The SAED pattern including both the ZnO nanowire and the Au particle is displayed in Figure 12b. The orientation relationship can be described as $(0001)_{\text{ZnO}} \parallel (111)_{\text{Au}}$, and $[01\bar{1}0]_{\text{ZnO}} \parallel [\bar{1}\bar{1}2]_{\text{Au}}$. After examining the lattice mismatch between ZnO and Au, the orientation relationship was chosen to minimize interface lattice mismatch. This fixed orientation relationship might be formed in the cooling process, during which the ZnO lattice decided the Au orientation when the Au changed from the liquid to solid state.

A recent study of Sn/ZnO has shown a different result.⁴⁸ Using tin particle guided growth of ZnO nanostructures as a model system, we have shown that the interfacial region of the tin particle with the ZnO nanowire/nanobelt could be ordered (or partially crystalline) during the VLS growth, although the local growth temperature is much higher than the melting point of tin, and the crystallographic lattice structure at the interface is important in defining the structural characteristics of the grown nanowires/nanobelts. The interface prefers to take the least lattice mismatch, thus, the crystalline orientation of the tin particle may determine the growth direction and the side surfaces of the nanowires/nanobelts. This result may have

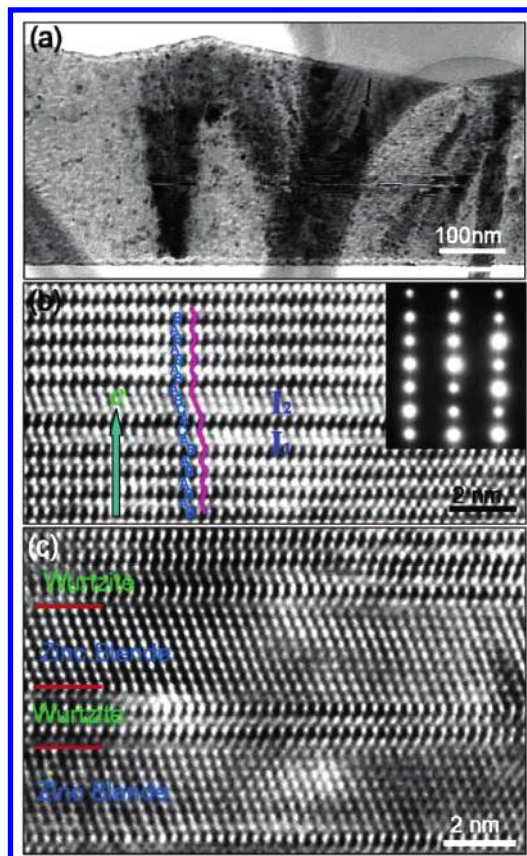


Figure 13. Nature of stacking faults (SFs). (a) Low-magnification TEM image of a ZnS belt. (b) and (c) HRTEM image of local area in (a) showing the existence of stacking faults and zinc blende phase. The stacking sequence and types of SFs are indicated.

important impact on the understanding of the physical and chemical process in VLS growth.

12. Planar Defects in Nanowires and Nanobelts

Planar defects are the most popular and most important defects in nanobelts. In some cases, the presence of planar defects is essential for stabilizing the surfaces that exhibit higher energies and leading the fastest anisotropic growth of the nanobelts along a specific direction. Planar defects can be twins and bicrystals, stacking faults, or an interstitial stacking layer introduced by impurity. The former two can be easily distinguished from the last two by electron diffraction. Quantitative image simulations are required to identify the nature of the stacking faults.

12.1 Stacking Faults. Stacking faults (SFs) are the most frequently observed planar defects in nanowires and nanobelts. SFs are formed by a change in stacking sequence of atomic planes. In the wurtzite structure, there are three possible types of stacking faults, I_1 , I_2 , and E in bulk materials, which are produced by extracting one layer, extracting two layers, and inserting a layer, respectively.^{49,50} The nature of stacking fault needs to be identified by combining HRTEM with image simulation. A low-magnification TEM image recorded from wurtzite-structured ZnS belt is given in Figure 13a, displaying some planar defects. HRTEM images from the defect regions are recorded in Figure 13b,c. The inserted SAED pattern in Figure 13b came from the area where the HRTEM image in Figure 13b was recorded. The c direction is marked in the image. The streaking along $[0001]$ direction in the SAED pattern is due to the shape effect of the planar defects in c plane. Despite

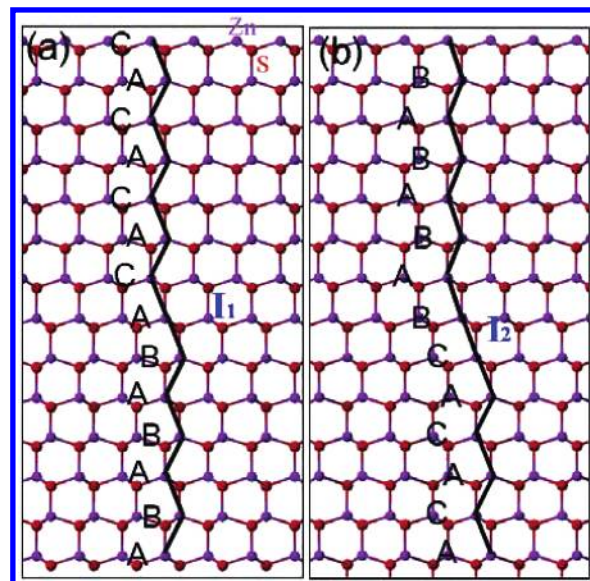


Figure 14. (a) and (b) the structural models of the I_1 and I_2 types stacking faults observed in Figure 13b,c, respectively.

the perfect ZnS wurtzite structure, corresponding to the **ABA-BAB** stacking sequence parallel to the (0001) plane, a new sequence identified as to be **...ABABCACABAB...** in the local area suggests the existence of I_1 and an I_2 stacking faults, as marked in the image. The **ABABAB** stacking sequence changes to **ABCABC** in some local area as shown in Figure 13(c), corresponding to the formation of the zinc blende phase in the wurtzite-matrix. The structural models of the I_1 and I_2 stacking faults are illustrated in Figure 14a,b, respectively. There is a $1/3[01\bar{1}0] + 1/2[0001]$ translation across the I_1 stacking fault, and a translation of $2/3[01\bar{1}0]$ across the I_2 stacking fault.

12.2 Twins and Bicrystals. Twin structure is most common in face-centered cubic structured metallic nanoparticles and silicon based nanowires. For wurtzite structures, there are possible twin boundaries defined by $(01\bar{1}1)$, $(01\bar{1}2)$ and $(01\bar{1}3)$.⁵¹ The theoretical calculations predicted that the $(01\bar{1}3)$ twin has the lowest energy, but there has no direct evidence about the existence of such a twin boundary in bulk crystals. By controlling the deposition conditions, twin nanobelts of wurtzite-structured ZnO and CdSe have been successfully synthesized. The most frequently observed twin structure takes the $(01\bar{1}3)$ twin plane, as expected theoretically. Nanowires/nanobelts with twin plane parallel to the growth direction are also called bicrystals, except that the two crystals have a fixed and specific orientation relationship.

Figure 15a shows a typical ZnO bicrystal. Its SAED pattern is displayed in Figure 15b, which is composed of two sets of diffraction spots that have symmetrical geometrical distribution but possibly variable intensity. The two set patterns are labeled using subscripts L and R specifying the left-hand and right-hand crystals, respectively. The common spot is the twin boundary plane $(01\bar{1}3)$, as indexed in the SAED pattern, and the incident beam direction is $[2110]$. The existence of high-density stacking faults in the dark-field image (Figure 15c) indicates the large local strain. The optimum orientation to image twins is parallel to the twin plane, so that the diffraction pattern shows mirror symmetry between the two sets of diffraction spots. Figure 16(a) is a HRTEM image recorded from the twin boundary, which clearly displays the mirror symmetry between the two crystals. HRTEM image simulation was carried out to clarify the Zn arrangement at the boundary. The best-matched structure model is depicted in Figure 16b. The simulated image

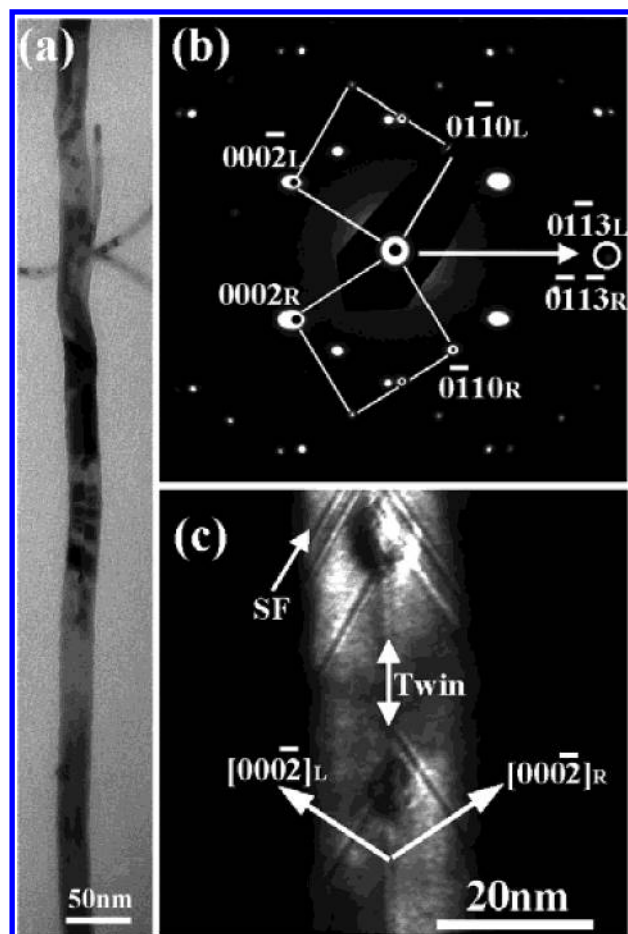


Figure 15. Twinned/bicrystal nanobelt of ZnO. (a) and (b) TEM image and corresponding SAED pattern of a ZnO nanobelt that has a (0113) twin parallel to the growth direction. (c) A dark-field TEM image showing the existence of stacking faults in the bicrystal nanobelt.

based on the model is inserted in Figure 16a. In the structure model, the red and purple spheres denote O and Zn ions, respectively. The two arrowheads indicate the positive [0001] direction. When we reverse the [0001] direction on both sides, the simulated image shows no difference, which means that HRTEM, at least at this resolution that is available in our laboratory, is insufficient to distinguish the polar direction of ZnO. However, no matter if the positive or negative [0001] direction is chosen, the detailed ions arrangement is preserved. For registration purpose, the yellow dots in the model and in the image indicate two corresponding points.

The (0113) twin structure has also been found in wurtzite-structured CdSe bicrystals. An SEM image presented in Figure 17a shows the bicrystal structure, with a sharp boundary at the center. The TEM image was recorded parallel to the twin plane so that the two crystals are symmetrically imaged (Figure 17b). The corresponding SAED pattern has two sets of diffraction spots and the fundamental units of the two are indicated. The common spot shared by the two sets of patterns is that from the twin plane, which is (0113) (Figure 17c). The incident electron beam is along $[2\bar{1}\bar{1}0]$. Figure 17d is a HRTEM image recorded from the twin boundary, which ambiguously presents the twin structure of the two sided crystals. High-density stacking faults also exist as indicated by arrowheads.

Besides (0113) twin structure, we also found the $(\bar{2}112)$ twin structure in ZnO bicrystal nanobelts. Figure 18a,b shows bright-field and dark-field images of the ZnO twinned nanobelts. The SAED pattern in Figure 18c indicates that the mirror plane of

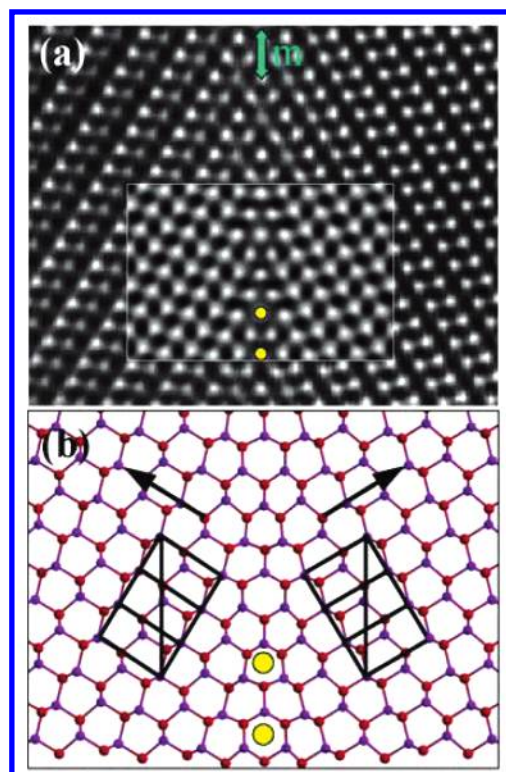


Figure 16. Atomic model of the twinned/bicrystal nanobelt. (a) HRTEM image of the (0113) twinned ZnO nanobelt, the inserted is a simulation image based on the model in (b). The following parameters chosen for the simulation: the sample thickness and defocus being 3.574 and 28.67 nm for JEOL 4000EX at 400 kV, respectively.

the twin structure is the $(\bar{2}112)$ plane. Only (0002) fringes can be observed in the HRTEM image, due to the interplanar distance of $(\bar{2}110)$ being smaller than the resolution of the microscope. The $\{\bar{2}112\}$ type of twins is responsible for the formation of tetrapole/tetraleq structures of ZnO.⁵² The diffraction contrast in Figure 18a,b indicates the large strain in the belt. Formation of stacking faults is an effective way to relax the strain.

Imaging twins must be carried out at proper orientation. The optimum orientation is parallel to the twin plan. For wurtzite structure, the beam direction is usually $[2\bar{1}\bar{1}0]$ and/or $[01\bar{1}0]$. For imaging stacking faults, the beam direction has to be chosen so that the displacement of the lattice is not parallel to the beam. The $[01\bar{1}0]$ direction for wurtzite may not be a good choice because the translation vectors \mathbf{R} of the stacking faults are $1/3[01\bar{1}0] + 1/2[0001]$ for I_1 and $2/3[01\bar{1}0]$ for I_2 .

12.3 Interstitial Stacking Layer Related Planar Defects.

For a general case, one-dimensional ZnO nanostructures without catalysts usually grow along the c -axis and the side surfaces are $\{01\bar{1}0\}$ and $\{2\bar{1}\bar{1}0\}$ due to their lower energies than that of (0001),⁵³ resulting in a vanishable dipole moment and much reduced piezoelectricity. To maximize the effect of polar surfaces and the piezoelectricity, nanobelts grow along $[01\bar{1}0]$ or $[2\bar{1}\bar{1}0]$ are preferred. We have previously reported ZnO nanobelts that grow along $[01\bar{1}0]$, and pointed out that the $[01\bar{1}0]$ nanobelts are always accompanied with basal plane stacking faults,^{53,54} which indicates the energy barrier set by the (0001) polar surfaces may be balanced by introducing basal-plane planar defects. To synthesize polar-surface dominated ZnO nanobelts, impurity atoms such as In were introduced in the source material to facilitate the formation of planar defects in the nanobelts. As a result, the $[01\bar{1}0]$ growth nanobelts were formed. An amazing thing is that some of the $[01\bar{1}0]$ growth

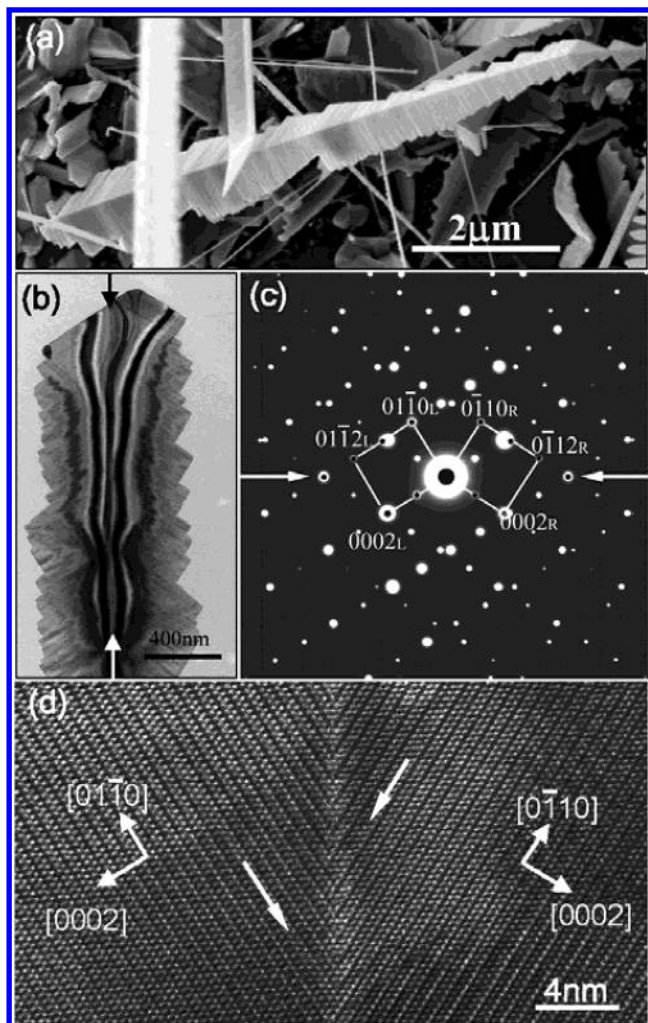


Figure 17. Twinned/bicrystal nanowire of CdSe. (a) SEM image CdSe (0113) twinned structure. (b) TEM image, (c) SAED pattern, and (d) the HRTEM image of the twin structure.

nanobelts can be self-coiling to form a complete nanoring structure.²³ Planar defects created by In doping have been suggested to be a mechanism for stabilizing the polar surface dominated nanobelts.⁵⁵

Figure 19a shows a ZnO nanobelt with planar defects parallel to the (0001) polar surfaces. Self-coiling of the polar nanobelt, driven by the electrostatic interaction between the polar surfaces, forms seamless, single-crystal nanorings (Figure 19b).²³ Energy-dispersive X-ray spectrum (EDS) recorded in TEM from the nanoring shows the presence of minor indium besides majority of Zn and O (Cu and Si signals come from the copper grid and the substrate) (Figure 19c). Quantitative analysis indicates the atomic ratio of $In:Zn \approx 1.15$, suggesting that In atoms are doped in the ZnO lattice. Combined our EDS results and the reports on the defect microstructure in indium doped ZnO ceramics,^{56–59} the planar defects in our nanobelts and nanorings may be related to a local segregation of In ions. The HRTEM image in Figure 19d is a nanobelt with two sharp-contrast planar defects, which is the building block of a nanoring. After constructing several possible structural models, we carried out some detailed image simulations in reference to the experimental data. If we consider the two dark layers (labeled I and II in the image) as two In–O octahedral layers, then we found the best-matched structural model is the one displayed in Figure 19e. If we define the (0001) surface as Zn-terminated and the (000 $\bar{1}$) surface as oxygen-terminated, so that the polarization is along c -axis, the two slabs

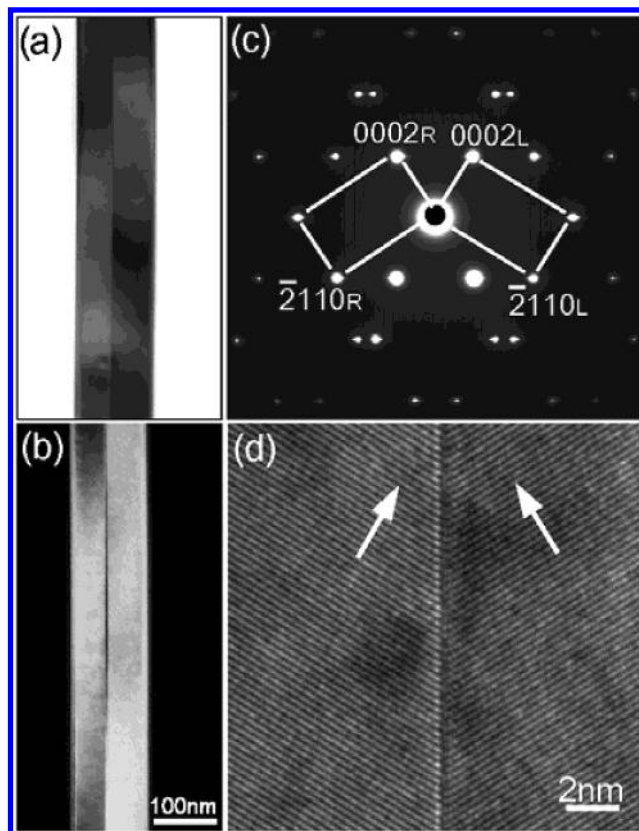


Figure 18. ZnO ($\bar{2}112$) twinned nanobelt. (a) and (b) are bright-field and dark-field TEM images, respectively. (c) SAED pattern, and (d) HRTEM image of the twin structure with the incidence electron beam along $[01\bar{1}0]$ direction.

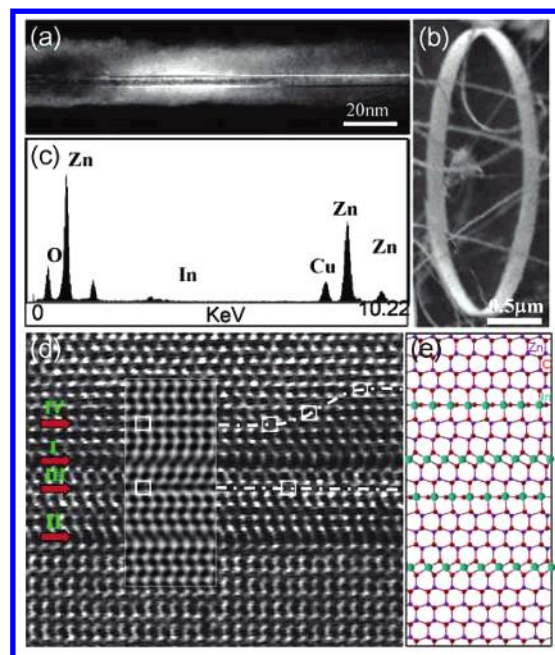


Figure 19. Planar defects created by doping. (a) Dark-field TEM image of ZnO nanobelt with planar defects. (b) SEM image of a ZnO nanoring formed by self-coiling of a nanobelt. (c) EDS spectrum showing the presence of In ions in the structure. (d) HRTEM image of the planar defects, and (e) the structural model. A simulated image is inserted in (d). The simulation is for a sample thickness of 2.924 nm, defocus -28.67 nm, for JEOL 4000EX at 400 kV.

of ZnO on both sides of the In–O octahedral layer must have opposite polarization, which means that the In–O layer effectively induces a “head-to-head” polarization domain, so-

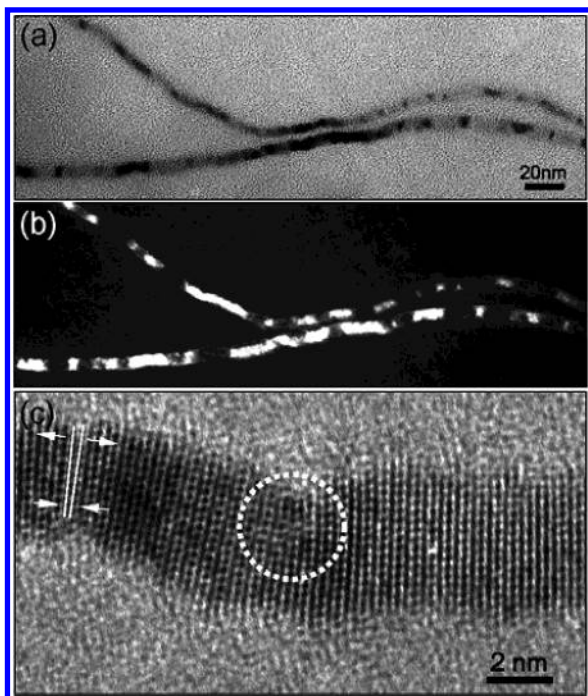


Figure 20. Dislocations in ultra-narrow nanobelts. (a,b) Bright-field and dark-field TEM images of ultrafine ZnO nanobelts. (c) HRTEM image indicating the existence of a dislocation.

called inversion domain boundary (IDB). To configure the two sharply contrasted planar defects (**I** and **II**), there must exist another type of defect (labeled as **III**) between the **I** and **II** layers, and it should correspond to a “tail-to-tail” IDB. The **III** layer does exist in the image, the bright spots forms a rectangle pattern, as indicated between the **I** and **II** layers. On the other hand, based on the structural model of In_2O_3 , the two slabs of ZnO on either sides of In–O octahedral layer can take not only head-to-head polarity, but also tail-to-tail polarity as presented in Figure 19e. In the first case, the 4-fold symmetry axis of the In–O octahedra lies in the ZnO *c*-plane to form a head-to-head IDB. In the second case, the 4-fold symmetry axis of the In–O octahedron is parallel to the *c*-axis to form a tail-to-tail IDB. Such tail-to-tail layer also exists above the **I** layer, as labeled to be the **IV** layer. This **IV** layer, however, seems not remain in a single *c*-plane, but moves across *c*-planes, as indicated by a dashed line. The transverse translation of the **IV** layer may be resulted from the relocation of the doped indium ions. It is worth noticing that the translation in the $[0001]$ direction across the tail-to-tail IDB is very small, and there is no translation along the $[01\bar{1}0]$ direction. A simulated image based on the model in Figure 19e is inserted in Figure 19d, which is An excellent match and supports our model.⁵⁵

13. Dislocations in Nanowires/Nanobelts

Not like stacking faults or twins, dislocations are rarely observed in nanowires and nanobelts, especially for oxides nanostructures. It may be due to the size effect, which makes the dislocations unstable in nanowires and nanobelts. In the past, almost all of the oxide nanostructures we have reported are free of dislocations. But recently, we have surprisingly observed dislocation in ultra-narrow ZnO nanobelts of 6 nm in width.⁶⁰ Figure 20a,b shows bright-field and dark-field images of two fine ZnO nanobelts, respectively. The variation of the contrast (especially in the dark-field image) reveals the nonuniform strain field distribution along the nanobelt, which may be created by the large deformation. The HRTEM image in Figure 20c reveals

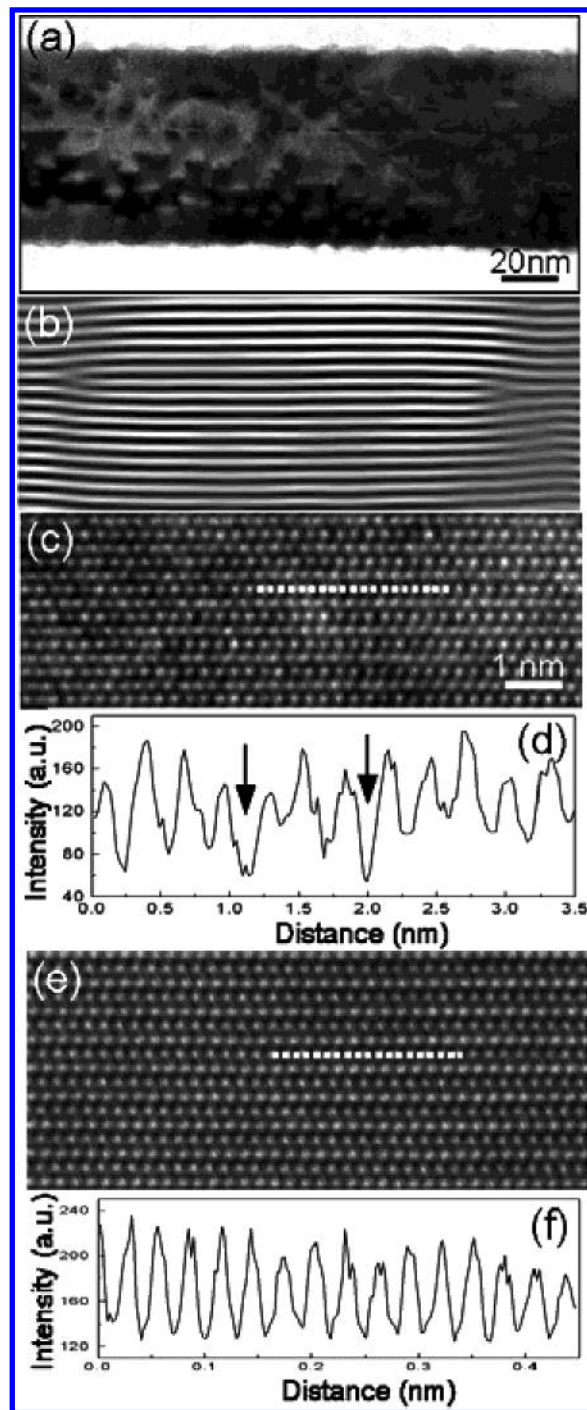


Figure 21. Imaging point defects in nanobelts. (a) Low magnification TEM image of a ZnO nanobelt doped with Mn, showing numerous mini-stacking faults produced by ion implantation. (b) Fourier filtered image showing a dislocation loop created by the mini-stacking fault. (c) HRTEM image of the as-implanted sample, and (d) intensity line scan parallel to the (0001) plane, showing fluctuation in image contrast due to ion implantation induced point defects. (e) HRTEM image of the implanted ZnO nanobelt after being annealed in oxygen to compensate the lost oxygen and the displaced cations, and (f) intensity line scan parallel to the (0001) plane, showing the disappearance of the fluctuation contrast in the image.

the existence of an edge dislocation with Burgers vector as $1/2[0001] + 1/3[01\bar{1}0]$ at the twisted area indicated by an circle. At the left-hand side of the nanobelt, no dislocation is formed, but the inter-planar distance is expanded to ~ 5.4 Å at the exterior arc and compressed to ~ 4.8 Å at the inner arc to accommodate the local strain. Such a gigantic change of $\sim 6\%$

in interplanar distance without fracture for oxide is only possible at nanoscale. The nonuniform deformation along these fine nanobelts corresponds to a nonuniform strain field. When the accumulated strain in some local areas is beyond the structural endurance, dislocations are introduced. This metallic like structural characteristic for oxides is unusual.

14. Point Defects in Nanobelts

Imaging of point defects is challenging for TEM. TEM imaging relies on diffraction and interference and it is much less sensitive to point defects distributed randomly or with a short range ordering. Oxygen deficient oxide nanostructures are of great interest because their conductivity depends on oxygen content. Although TEM cannot be directly applied to determine oxygen deficiency in ZnO nanostructures, it may help in other cases. We have recently applied TEM to directly image defects created in ZnO nanobelts by Mn doping.⁶¹ The Mn doping was carried out using an ion implantation at 30 keV at a flux of $1 \times 10^{15} \text{ cm}^{-2}$. A high density of mini-stacking faults is created (Figure 21a). Taking a Fourier transform of a HRTEM image and select only the $\pm(0002)$ diffraction spots by a filter, an inverse Fourier transform gives the distribution of the (0002) fringes in the image (Figure 21b), which clearly displays the mini-stacking fault.

Figure 21c is a HRTEM image recorded from an as-implanted ZnO nanobelt. A line scan along the dashed line gives an intensity profile across the atomic columns along $[01\bar{1}0]$. An ideal profile should be periodic with equal amplitude. The large-scale change in the image contrast from column to column (see Figure 21d) reflects the introduction of point defects as well as lattice distortion due to ion damage. The point defects can be oxygen deficiency and cation interstitials. After annealing the sample in air, the image contrast is very uniform (see Figures 21e,f), because of the disappearance of the point defects.

15. Summary

Structure analysis of one-dimensional (1D) nanostructures has some differences from the analysis of nanoparticles. This paper is about the application of high-resolution TEM for properly determining the structures of 1D nanostructures, aiming at providing a guidance and practical examples for readers who are interested in nanowire and nanobelt structures. It is known that structural control is the key for property control. Using ZnO, CdSe, and ZnS as examples, we have illustrated the technical details of how to use transmission electron microscopy for correctly analyzing the structure of nanowires and nanobelts, including growth direction, side/top surfaces, surface polar direction, surface reconstruction, point defects, dislocations, planar defects, and twin/bicrystals. The methodologies introduced here can be applied to a wide range of 1D nanostructures.

Acknowledgment. Thanks to P. X. Gao, W. L. Hughes, X. Y. Kong, C. Ma, D. Moore, X. D. Wang, R. S. Yang, C. Ronning, and J. M. Zuo for their collaboration for the work reviewed in this article. We acknowledge generous support by the Defense Advanced Projects Research Agency, National Science Foundation, and NASA.

References and Notes

- (1) Wang, Z. L., Ed.; *Nanowires and Nanobelts, Vol. I: Metal and Semiconductor, Nanowires*; Kluwer Academic Publisher: New York, 2003.
- (2) Wang, Z. L., Ed.; *Nanowires and Nanobelts, Vol. II: Nanowires and Nanobelts of Functional Materials*; Kluwer Academic Publisher: New York, 2003.

- (3) Tenne, R.; Homyonfer, M.; Feldman, Y. *Chem. Mater.* **1998**, *10*, 3225.
- (4) Saito, Y.; Matsumoto, T. *Nature* **1998**, *392*, 237.
- (5) Gao, P. X.; Wang, Z. L. *J. Am. Chem. Soc.* **2003**, *125*, 11 299.
- (6) Trentler, T. J.; Hickman, K. M.; Goel, S. C.; Viano, A. M.; Gibbons, P. C.; Buhro, W. E. *Science* **1995**, *270*, 1791.
- (7) Morales, A. M.; Lieber, C. M. *Science* **1998**, *279*, 208.
- (8) Lee, S. T.; Wang, N.; Zhang, Y. F.; Tang, Y. H. *MRS Bull.* **1999**, *24*, 36.
- (9) Chen, C. C.; Yeh, C. C.; Chen, C. H.; Yu, M. Y.; Liu, H. L.; Wu, J. J.; Chen, K. H.; Chen, L. C.; Peng, J. Y.; Chen, Y. F. *J. Am. Chem. Soc.* **2001**, *123*, 2791.
- (10) Pan, Z. W.; Dai, Z. R.; Ma, C.; Wang, Z. L. *J. Am. Chem. Soc.* **2002**, *124*, 1817.
- (11) Dai, H. J.; Wong, E. W.; Lu, Y. Z.; Fan, S. S.; Lieber, C. M. *Nature* **1995**, *375*, 769.
- (12) Manna, L.; Scher, E. C.; Alivisatos, A. P. *J. Am. Chem. Soc.* **2000**, *122*, 12 700.
- (13) Link, S.; El-Sayed, M. A. *J. Appl. Phys.* **2002**, *92*, 6799.
- (14) Huynh, W. U.; Dittmer, J. J.; Alivisatos, A. P. *Science* **2002**, *295*, 2425.
- (15) Lao, J. Y.; Huang, J. Y.; Wang, D. Z.; Ren, Z. F. *Nano Lett.* **2003**, *3*, 235.
- (16) Zhang, Y.; Suenaga, K.; Colliex, C.; Iijima, S. *Science* **1998**, *281*, 973.
- (17) Wang, Z. L.; Dai, Z. R.; Gao, R. P.; Bai, Z. G.; Gole, J. L. *Appl. Phys. Lett.* **2000**, *77*, 3349.
- (18) Pan, Z. W.; Dai, Z. R.; Wang, Z. L. *Science* **2001**, *291*, 1947.
- (19) Wang, Z. L.; Pan, Z. W.; Dai, Z. R. US Patent No. 6,586,095.
- (20) Dai, Z. R.; Pan, Z. W.; Wang, Z. L. *J. Phys. Chem. B* **2002**, *106*, 902.
- (21) Dai, Z. R.; Pan, Z. W.; Wang, Z. L. *J. Am. Chem. Soc.* **2002**, *124*, 8673.
- (22) Kong, X. Y.; Wang, Z. L. *Nano Lett.* **2003**, *3*, 1625.
- (23) Kong, X. Y.; Ding, Y.; Yang, R. S.; Wang, Z. L. *Science* **2004**, *303*, 1348.
- (24) Gao, P. X.; Wang, Z. L. *J. Phys. Chem. B* **2004**, *108*, 7534.
- (25) Wang, Z. L.; Hui, C., Eds.; *Electron Microscopy of Nanotubes*; Kluwer Academic Publisher: New York, 2003.
- (26) Berta, Y.; Ma, C.; Wang, Z. L. *Micron* **2002**, *33*, 687.
- (27) Dai, Z. R.; Pan, Z. W.; Wang, Z. L. *Solid State Comm.* **2001**, *118*, 351.
- (28) Wu, Y.; Cui, Y.; Huynh, L.; Barrelet, C. J.; Bell, D. C.; Lieber, C. M. *Nano Lett.* **2004**, *4*, 433.
- (29) Wang, Z. L.; Mohamed, M.; Link, S.; El-Sayed, M. A. *Surf. Sci.* **1999**, *440*, L809.
- (30) Wang, Z. L.; Kang, Z. C. *Functional and Smart Materials Structural Evolution and Structure Analysis*; Plenum Press: New York, 1998.
- (31) Spence, J. C. H.; Zuo, J. M. *Electron Microdiffraction*; Plenum Press: New York, 1992.
- (32) Buxton, B. F.; Eades, J. A.; Steeds, J. W.; Rackham, G. M. *Philos. Trans. R. Soc. London* **1976**, *281*, 171.
- (33) Tanaka, M.; Terauchi, M.; Kaneyama, T. *Convergent beam Electron Diffraction I-III*; JEOL: Tokyo, 1988.
- (34) Wang, Z. L.; Kong, X. Y.; Zuo, J. M. *Phys. Rev. Lett.* **2003**, *91*, 185 502.
- (35) Zuo, J. M.; Mabon, J. C. WebEMAPS software, University of Illinois at Urbana - Champaign; URL: <http://emaps.mrl.uiuc.edu/>.
- (36) Yang, R. S.; Ding, Y.; Wang, Z. L. *Nano Lett.* **2004**, *4*, 1309.
- (37) Wang, Z. L. *J. Phys. Chem. B* **2000**, *104*, 1153.
- (38) Dulub, O.; Boatner, L. A.; Diebold, U. *Surface Sci.* **2002**, *519*, 201.
- (39) Gao, P. X.; Ding, Y.; Wang, Z. L. *Nano Lett.* **2003**, *3*, 1315.
- (40) Wagner, R. S.; Ellis, W. C. *Appl. Phys. Lett.* **1964**, *4*, 89.
- (41) Wu, Y. Y.; Yang, P. D. *J. Am. Chem. Soc.* **2001**, *123* (13), 3165.
- (42) Morales, A. M.; Lieber, C. M. *Science* **1998**, *279*, 208.
- (43) Huang, M. H.; Wu, Y. Y.; Feick, H. N.; Weber, Tran, E.; Yang, P. D. *Adv. Mater.* **2001**, *13*, 113.
- (44) Liang, C. H.; Zhang, L. D.; Meng, G. W.; Wang, Y. W.; Chu, Z. Q. *J. Non-Crystalline Solids* **2000**, *277*, 63.
- (45) Zhu, Y. Q.; Hsu, W. K.; Terrones, M.; Grobert, N.; Terrones, H.; Hare, J. P.; Kroto, H. W.; Walton, D. R. M. *J. Mater. Chem.* **1998**, *8*, 1859.
- (46) Choi, Y. C.; Kim, W. S.; Park, Y. S.; Lee, S. M.; Bae, D. J.; Lee, Y. H.; Park, G. S.; Choi, W. B.; Lee, N. S.; Kim, J. M. *Adv. Mater.* **2000**, *12*, 746.
- (47) Pan, Z. W.; Dai, Z. R.; Ma, C.; Wang, Z. L. *J. Am. Chem. Soc.* **2002**, *124*, 1817.
- (48) Ding, Y.; Gao, P. X.; Wang, Z. L. *J. Am. Chem. Soc.* **2004**, *126*, 2066.
- (49) Potin, V.; Ruterana P.; Nouet, G. *J. Phys.: Condens. Matter* **2000**, *12*, 10 301.

- (50) Stampfl, C.; Van de Walle, C. G. *Phys. Rev. B* **1998**, 57, R15052.
- (51) Béré, A.; Serra, A. *Phys. Rev. B* **2003**, 68, 033305.
- (52) Dai, Y.; Zhang, Y.; Wang, Z. L. *Solid State Commu.* **2003**, 126, 629.
- (53) Pan, Z. W.; Dai, Z. R.; Wang, Z. L. *Science* **2001**, 291, 1947.
- (54) Wang, Z. L.; Pan, Z. W.; Dai, Z. R. *Microsc. Microanal.* **2002**, 8, 467.
- (55) Ding, Y.; Kong, X. Y.; Wang, Z. L. *Phys. Rev. B* **2004**, submitted.
- (56) Yan, Y.; Pennycook, S. J.; Dai, J.; Chang, R. P. H.; Wang, A.; Marks, T. J. *Appl. Phys. Lett.* **1998**, 73, 2585.
- (57) McCoy, M. A.; Grimes, R. W.; Lee, W. E. *Philos. Mag. A* **1997**, 76, 1187.
- (58) Cannard P. J.; Tilley R. J. D. *J. Solid Stat. Chem.* **1988**, 73, 418.
- (59) Li, C.; Bando, Y.; Nakamura, M.; Kimizuka, N. *Micron* **2000**, 31, 543.
- (60) Wang, X. D.; Ding, Y.; Summers, C. J.; Wang, Z. L. *J. Phys. Chem. B* **2004**, 108, 8773.
- (61) Ronning, C.; Gao, P. X.; Ding, Y.; Wang, Z. L. *Appl. Phys. Lett.* **2004**, 84, 783.